Electronic Research Archive

https://www.aimspress.com/journal/era

ERA, 34(2): 1173–1194.
DOI: 10.3934/era.2026054
Received: 13 November 2025
Revised: 01 January 2026
Accepted: 12 January 2026
Published: 05 February 2026

Research article

Multimodal bifurcation control of parkinsonian beta oscillations by pedunculopontine nucleus pathways: A unified computational framework revealing dynamic therapeutic targets

Bing Hu[1,*], **Pinyi Ye**[2], **Yuting Zhang**[1], **Te Nan**[1] **and Xiaoye Shi**[1]

[1] Department of Mathematics, School of Mathematical Sciences, Zhejiang University of Technology, Hangzhou 310023, China

[2] College of Information Engineering, Zhejiang University of Technology, Hangzhou 310023, China

* **Correspondence:** Email: djhubingst@163.com.

Abstract: This study introduces a novel cortico-thalamo-basal ganglia-pedunculopontine nucleus (PPN) (CTBGP) computational framework to investigate how PPN-related pathways control beta oscillations. We observe that PPN-thalamic pathways exert bidirectional Hopf bifurcation control over thalamic beta oscillations, with coupling strength adjustments shifting stable/oscillatory state boundaries; PPN-cortical projection stabilizes cortical beta oscillations through supercritical/subcritical Hopf transitions dependent on coupling strength; PPN-GPi projection modulates cortico-thalamic beta oscillations via interactions with GABAergic GPi-thalamic pathways, enabling coexistence of supercritical/subcritical bifurcations; PPN-STN projection strongly suppress basal ganglia beta oscillations by elevating STN-GPe network activity to saturated states. Notably, three direct PPN inputs (EPN-PPN, STN-PPN, GPi-PPN) collectively regulate beta oscillations through the PPN-STN-GPe axis. This work provides the computational evidence that PPN pathways dynamically control beta oscillations across CTBG subcircuits via bifurcation mechanisms. The identified PPN-STN-GPe axis and thalamic/cortical projections offer novel targets for DBS and pharmacological interventions.

Keywords: pedunculopontine nucleus; cortical-thalamic-basal ganglia circuit; Parkinson's beta oscillation; Hopf bifurcation

1. Introduction

Parkinson's disease (PD) is a prevalent neurodegenerative disorder characterized by motor symptoms such as tremor, rigidity, and bradykinesia [1]. At the neural circuit level, abnormal beta-band oscillations (βOS) (13–30 Hz) in the basal ganglia (BG) have emerged as a key

pathophysiological hallmark [2, 3]. These oscillatory activities are thought to disrupt the normal information processing within the BG-thalamo-cortical loop, leading to motor dysfunction [4].

There are currently multiple hypotheses regarding the origin of βOS [5, 6]: First, the thalamic circuit origin hypothesis posits that abnormal discharges in certain thalamic nuclei or abnormal connections with the BG trigger βOS. Second, the cortical circuit origin hypothesis emphasizes that abnormal cortical inputs lead to changes in neuronal activity patterns within the BG, thereby inducing βOS. Third, the BG circuit origin hypothesis points out that an imbalance in neuronal network activity within the BG, particularly abnormal dopamine regulation between the direct and indirect pathways, is crucial for the generation of βOS. Finally, the cortico-thalamo-basal ganglia (CTBG) circuit origin hypothesis integrates the above viewpoints, suggesting that abnormalities in any part of this circuit can ultimately lead to the generation of βOS within the BG through interactions among circuits. In-depth study of these hypotheses contributes to a more comprehensive understanding of the pathological mechanisms of PD and provides theoretical foundations for developing new treatment strategies. Currently, numerous CTBG computational models have been employed to explore the dynamical mechanisms underlying the origin of βOS [7–9]. In addition, it is noteworthy that certain optimization algorithms and machine learning models hold significant guiding value for the early detection of PD [10, 11].

In recent years, the role of the pedunculopontine nucleus (PPN) in the pathological mechanisms and motor regulation of PD has gradually gained attention [12, 13]. As a crucial component of the midbrain motor region, the PPN is closely associated with axial symptoms, such as postural instability and gait disorders in PD patients [14]. Clinical studies have demonstrated that low-frequency electrical stimulation of the PPN in PD patients can effectively alleviate their axial symptoms, suggesting that the PPN may become a novel therapeutic target for gait disorders in PD [15–17]. Further research has revealed that under PD conditions, the electrical activity of the PPN becomes abnormal, with changes in both its firing frequency and firing pattern [18, 19]. This may be related to the functional inhibition of the PPN caused by abnormalities in the BG circuitry [18, 19].

In terms of anatomical connectivity, the PPN has complex fiber connections with tissues, such as the cortex, thalamus, and BG [20]. The PPN directly receives efferent signals from the cerebral cortex and transmits them to the thalamus, brainstem, and spinal motor areas, participating in motor regulation and muscle tone modulation [20, 21]. There are extensive neural projections between the PPN and the BG, with the BG forming interconnected neural circuits with the PPN through structures such as the subthalamic nucleus (STN) and globus pallidus (GP), jointly regulating motor rhythm and postural balance [19]. In addition, the PPN has bidirectional fiber connections with the thalamus, participating in the processing of sensory information and the regulation of motor output [22, 23]. These complex connection structures enable the PPN to play a crucial role in the pathological mechanisms of PD. In-depth research on the connection structures between the PPN and these tissues, as well as their pathophysiological changes in PD, will help elucidate the occurrence mechanisms of axial symptoms in PD and provide a theoretical basis for the development of precise therapeutic approaches targeting the PPN [12, 24]. However, the dynamic mechanisms underlying the PPN's regulation of Parkinsonian oscillations remain unclear, and relevant computational model studies are still insufficient.

In our latest study, we developd four CTBG computational models to explore the genesis and regulatory mechanisms underlying βOS [9]. Our findings demonstrate that alterations in coupling weights trigger these oscillations through Hopf bifurcations, while the GP (both the medial part and

lateral part) exerts bidirectional regulatory influences on them. Additionally, both external electrical stimulation and deep brain stimulation (DBS) effectively suppress these oscillations, thereby underscoring the GP as promising target for DBS and offering valuable insights into the regulation of βOS within the CTBG framework.

Based on four hypotheses regarding the origin of βOS [5, 6], this paper establishes four cortico-thalamo-basal ganglia-PPN (CTBGP) computational models to systematically investigate the dynamic roles of projections directly connected to the PPN in controlling PD. Our main conclusions are as follows: the two direct glutamatergic (GLU) projections from the PPN to the thalamus can effectively regulate βOS in the thalamus; both an increase and a decrease in coupling strength in the GLU PPN-cortical projection could potentially push the cortical βOS into the stable state via Hopf bifurcation; the GLU PPN-GPi (internal segment of the GP) projection exerts a bidirectional Hopf bifurcation control effect on βOS induced via the cortico-thalamic circuit, through the interaction between the two GABAergic (GABA) GPi-thalamus projections; the GLU PPN-STN projection plays a significant role in controlling βOS within the BG; the three direct input pathways of the PPN can inhibit βOS in the BG through the PPN-STN projection; in the two-dimensional parameter space, the coupling strengths in the aforementioned projections adjust βOS and the stable region by shifting the Hopf bifurcation curves; the results further elucidate the role of the PPN in regulating PD, and provide computational evidences for targeting the PPN as an intervention strategy for PD.

We introduce the CTBGP model and methodology in Section 2. In Section 3, we provide a detailed analysis of the main results. Finally, we discuss the findings of this paper in Section 4.

2. Materials and methods

2.1. The CTBGP network

The CTBGP network comprises two parts: the CTBG circuit and the PPN (Figure 1). The structure of the CTBG circuit is similar to that of previous PD computational models [5, 6, 9], and a brief introduction is provided here. The CTBG network is composed of two parts: the BG and the cortico-thalamic circuit. The BG comprises five nuclei: the STN, striatal D1 (SD1), striatal D2 (SD2), the GPi, and the external segment of the GP (GPe). The cortico-thalamic circuit comprises four nuclei: the cortical excitatory nucleus (EPN), cortical inhibitory nucleus (IIN), thalamic relay nucleus (SRN), and thalamic reticular nucleus (TRN). We hypothesize that the projections between nuclei are mediated by excitatory GLU (arrows) and inhibitory GABA (dots), respectively. Specifically, there are self-feedback projections in the EPN, IIN, SD1, SD2, and GPe nuclei. The connection structures between various nuclei adopted in the model are all based on published neuroanatomical and electrophysiological experimental evidence. Specifically, for the BG circuit, SD1 and SD2 project to GPi and GPe through the direct and indirect pathways, respectively, both of which are GABAergic inhibitory connections; STN sends GLU excitatory projections to GPi and GPe, while GPe provides GABAergic feedback inhibition to STN [5, 6]. For the CT circuit, EPN sends GLU projections to SRN and TRN, SRN has GLU projections to both TRN and EPN, and TRN provides GABAergic inhibitory feedback to SRN, forming the classic cortical-thalamic feedback circuit [5, 6].

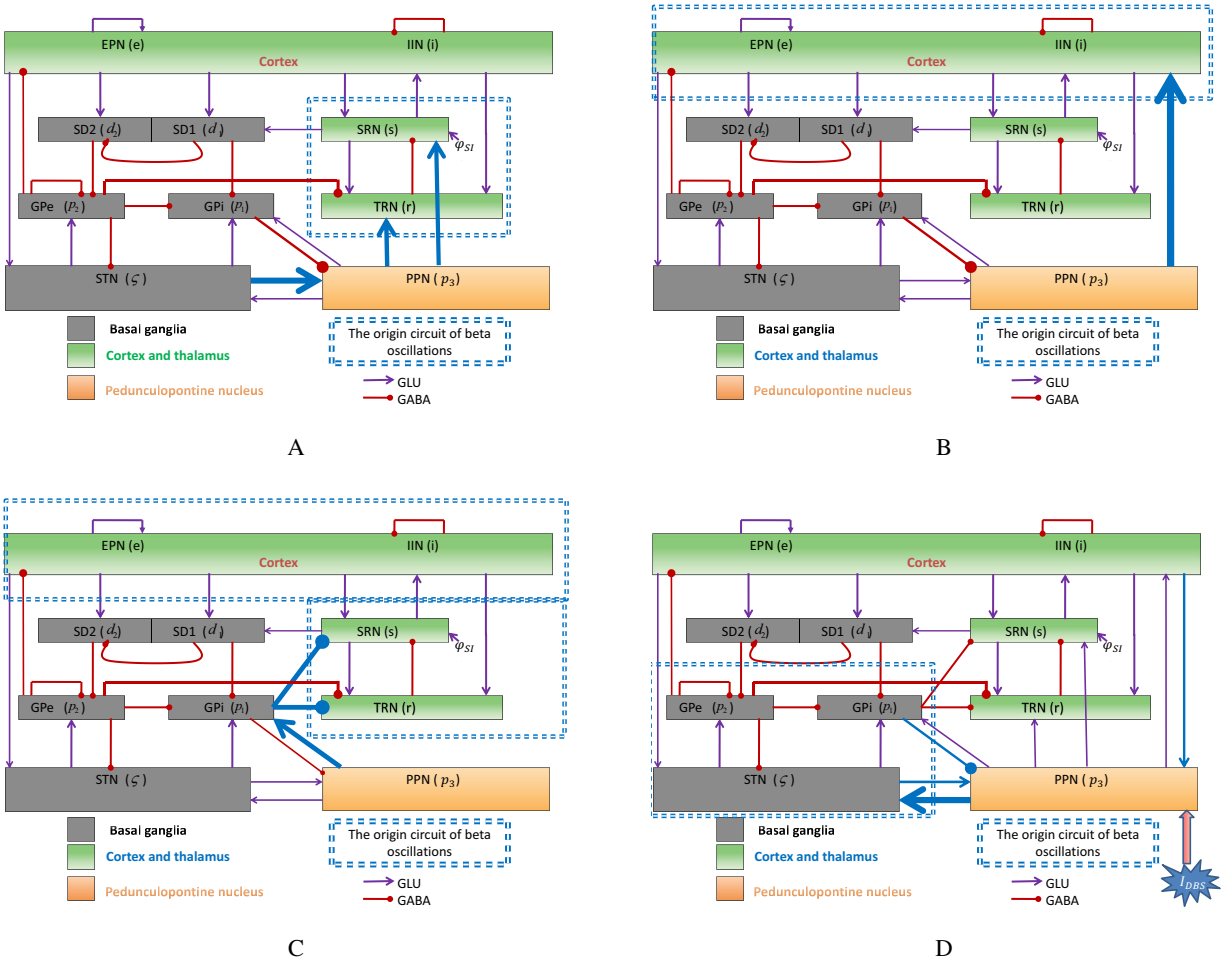

Figure 1. The CTBGP connection structure. The cortex contains two nuclei: EPN (e) and IIN (i). The thalamus contains two nuclei: SRN (s) and TRN (r). EPN, IIN, SRN, and TRN constitute the cortical-thalamic circuit. BG comprises five nuclei: SD1 (d_1), SD2 (d_2), STN (ζ), GPe (p_2), and GPi (p_1). We hypothesize that the projections between nuclei are mediated by excitatory GLU (arrows) and inhibitory GABA (dots), respectively. Specifically, there are self-feedback projections in the EPN, IIN, SD1, SD2 and GPe nuclei. To distinguish the different origin locations of βOS and the different control mechanisms of PPN, we classify the CTBGP connection structure into four types: CTBGP1 (A), CTBGP2 (B), CTBGP3 (C), and CTBGP4 (D). In (A), we hypothesize that βOS originates from the thalamic circuit and consider the controlling effects of the STN-PPN projection and the PPN-thalamic projection on βOS. In (B), we hypothesize that βOS originates from the cortical circuit and consider the possible regulatory effect of the PPN-EPN projection on βOS. In (C), we assume that βOS originates from the cortical-thalamic circuit and investigate the regulatory effects of the PPN-GPi projection and the GPi-thalamic projection on βOS. In (D), we assume that βOS is caused by abnormal interactions within the BG circuit and consider the inhibitory effects of the PPN-STN projection and related projections on βOS.

Furthermore, the connections between the PPN and the CTBG circuit are referenced based on the

anatomical structure and experimental evidence of the PPN. Anatomically, the PPN has extensive reciprocal projections with the STN and GPi [20]. The PPN exerts significant GLU projections onto the STN and GPi, while simultaneously receiving GLU input from the STN and GABA input from the GPi, as shown in Figure 1(A). Through functional and anatomical investigations, evidence has emerged indicating that the PPN modulates activity within thalamic structures, including the reticular formation and intralaminar nuclei [23]. Thus, in the CTBGP model, we assume that the PPN has direct GLU outputs to both the SRN and the TRN (Figure 1(A)). On the other hand, a substantial amount of experimental evidence indicates that there is reciprocal direct communication between the PPN and the cortex [20, 25], and that the interaction between the PPN and the cortex plays a crucial role in PD [19, 25]. So, in the CTBGP model, we assume that there are direct reciprocal GLU projections between the PPN and the EPN (Figure 1(D)).

In order to specifically analyze the functions of different pathways related to PPN in controlling PD, we divide the CTBGP model into four types: CTBGP1 (Figure 1(A)), CTBGP2 (Figure 1(B)), CTBGP3 (Figure 1(C)), and CTBGP4 (Figure 1(D)). In the CTBGP1 model, we hypothesize that βOS originates from the thalamic circuit and consider the controlling effects of the STN-PPN projection and the PPN-thalamic projection on βOS. In the CTBGP2 model, we hypothesize that βOS originates from the cortical circuit and consider the possible regulatory effect of the PPN-EPN projection on βOS. In the CTBGP3 model, we assume that βOS originates from the cortical-thalamic circuit and investigate the regulatory effects of the PPN-GPi projection and the GPi-thalamic projection on βOS. In the CTBGP4 model, we assume that βOS is caused by abnormal interactions within the BG circuit and consider the inhibitory effects of the PPN-STN projection and related projections on βOS.

2.2. Equation description

The foundational element is the population-centered model created by Robinson et al. [26, 27], which was subsequently advanced through research on computational models for epilepsy [28–30] and PD [5, 6, 9]. A more detailed description of the equations can be found in [5, 6], and we provide a brief description of the key information.

In brief, the module is comprised of ten distinct groups of neurons: EPN (e), IIN (i), SRN (s), TRN (r), SD1 (d_1), SD2 (d_2), STN (ζ), GPe (p_2), GPi (p_1), and PPN (p_3). Every population possesses two state parameters: an average potential denoted as V and an average firing frequency represented by ϕ (in Hz). Regarding every population, the average potential V undergoes temporal changes, shaped by the inputs it receives not only from within itself, but also from the remaining populations. The effect that the population x exerts on a specific target population y is dictated by a coupling weight ν_{yx}, $(x, y \in \{e, i, s, r, d_1, d_2, \zeta, p_2, p_1, p_3\})$. Excitatory connections correspond to positive coupling weights $(\nu_{yx} > 0)$, indicating that such inputs will elevate the average membrane potential of the target nucleus, thereby increasing its firing rate; in contrast, inhibitory connections correspond to negative coupling weights $(\nu_{yx} < 0)$, signifying that such inputs will reduce the average membrane potential of the target nucleus, thus suppressing its activity. There exist connections exhibiting positive coupling intensities originating from the EPN, SRN, STN, and PPN; meanwhile, connections displaying negative coupling intensities are found emanating from the IIN, TRN, SD1, SD2, GPe, and GPi.

For the population $\varpi(\varpi \in \{e, i, s, r, d_1, d_2, \zeta, p_2, p_1, p_3\})$, the average potential V_ϖ is associated with

the cumulative total of the incoming signals through the application of a differential operator $\mathbb{G}$,

$$\mathbb{G}V_{\varpi}(t) = \Sigma_{\delta\in\mathcal{J}} v_{\varpi\delta}.\phi_{\delta}(t-\tau_{\varpi\delta}), \tag{2.1}$$

where the expression for the difference-quantifying operator $\mathbb{G}$ is defined as

$$\mathbb{G} = \frac{1}{\varphi\psi}[\frac{\partial^2}{\partial t^2} + (\varphi+\psi)\frac{\partial}{\partial t} + \varphi\psi]. \tag{2.2}$$

In Eq (2.1), $\mathcal{J}$ represents the assembly of every nucleus that delivers direct synaptic signals to the nucleus denoted as "ϖ". To streamline the calculations without compromising the qualitative dynamic analysis, the delay parameters $\tau_{\varpi\delta}$ are postulated to be zero across all pathways within the CTBGP model. Concerning the differential operator presented in Eq (2.2), the parameters φ and ψ are deliberately picked to ensure that its impulse response closely resembles the temporal evolution pattern of a synaptic potential.

To fully flesh out the model's depiction, it is essential to clarify the manner in which the firing frequency of a population ϕ_{ϖ} is contingent upon its average potential V_{ϖ}. For populations comprising neurons that are relatively closely packed together, where the transmission of signals is constrained (denoted as $\kappa(\kappa \in \{i, s, r, d_1, d_2, \zeta, p_2, p_1, p_3\})$), this correlation is presumed to follow a sigmoid-shaped function,

$$\phi_{\kappa}(t) = P_{\kappa}[V_{\kappa}(t)] = \frac{P_{\kappa}^{\max}}{1+\exp[-\frac{\pi}{\sqrt{3}}\frac{V_{\kappa}(t)-\vartheta_{\kappa}}{\sigma}]}. \tag{2.3}$$

where P_{κ} is the firing rate, $P_{\kappa}^{\max}$ embodies the highest possible firing rate that can be reached, ϑ_{κ} symbolizes the typical firing threshold value, and σ serves as the indicator of the spread or variability in the threshold distribution among the nucleus.

Specifically, in the case of the EPN, it is postulated that potentials spread in a manner akin to wave propagation. For solutions that are uniform across space (the sole type under examination in this context), this presumption results in

$$\frac{1}{\gamma_e^2}[\frac{\partial^2}{\partial t^2} + 2\gamma_e\frac{\partial}{\partial t} + \gamma_e^2]\phi_e(t) = P_e(t), \tag{2.4}$$

$\gamma_e = v_e/r_e$ represents the quotient of the propagation speed to the average length of axons, v_e signifies the propagation speed, and r_e indicates the mean length of axons in EPN.

Furthermore, the potential of the IIN is subordinate to, or follows the same pattern as, that of the EPN, which can be expressed as $V_i = V_e$. Consequently, in our numerical computations, we also make the assumption that $P_i = P_e$.

In the subsequent analysis, we examine not only the qualitative attributes of the solutions to the system of equations outlined in Eqs (2.1)–(2.4), but also the spectral properties of these solutions. Ultimately, by transforming second-order operators into first-order ones, we derive a set of four coupled differential equations that describe the CTBGP model (refer to the Appendix).

2.3. Data origins and processing techniques

All the default parameter values within the CTBGP model are drawn from plausible physiological ranges [27] and have been validated through prior experimental and computational investigations (see Table 1 for details). During numerical computations, most parameters are set to their default values; however, a small number of parameters are adjusted to values near the defaults based on the requirements of the analysis.

Table 1. Default settings for parameters in the CTBGP model, detailed origins of these can be found in [5, 9, 28, 31].

$\nu_{p_3p_1}$	ν_{rp_3}	ν_{ep_3}	ν_{d_1e}	ν_{sp_3}	$\nu_{p_3\zeta}$	$\nu_{p_1p_3}$	Unit
−0.0301	0.032	0.45	1.01	0.032	0.1	0.42	mV s
$\nu_{p_1\zeta}$	ν_{ee}	ν_{d_2e}	ν_{rp_1}	ν_{d_2s}	$\nu_{p_1p_2}$	ν_{ei}	Unit
0.299	1.01	0.699	−0.03499	0.04997	−0.02996	−1.801	mV s
ν_{se}	$\nu_{p_2\zeta}$	ν_{sp_1}	$\nu_{p_2p_2}$	$\nu_{\zeta e}$	$\nu_{d_1d_1}$	ν_{es}	Unit
2.202	0.4499	−0.03499	−0.07501	0.101	−0.2002	1.7993	mV s
$\nu_{p_1d_1}$	ν_{ep_2}	ν_{d_1s}	ν_{rp_2}	ν_{sr}	$\nu_{d_2d_2}$	$\nu_{\zeta p_2}$	Unit
−0.0999	−0.0498	0.1001	−0.0498	−2	−0.2998	−0.04002	mV s
ν_{p_3e}	$\nu_{\zeta p_3}$	ν_{rs}	ν_{re}	$\nu_{p_2d_2}$			Unit
0.45	1.5	0.501	0.05001	-0.2998			mV s
$P_s^{\max}$	$P_{d_1}^{\max}$	$P_{p_3}^{\max}$	$P_{p_2}^{\max}$	$P_r^{\max}$	$P_{p_1}^{\max}$	$P_{d_2}^{\max}$	Unit
249.98	64.99	200.2	299.9	249.98	250.1	65.01	Hz
$P_e^{\max}, P_i^{\max}$	$P_\zeta^{\max}$						Unit
250.1	500.1						Hz
ϑ_r	ϑ_{d_2}	ϑ_{d_1}	ϑ_s	ϑ_{p_2}	ϑ_{p_3}	ϑ_e, ϑ_i	Unit
14.98	19.02	18.99	14.98	9.01	9.01	15.01	mV
ϑ_{p_1}	ϑ_ζ						Unit
10.01	9.99						mV
φ_{SI}	φ	σ	ψ	γ_e			
2.01 mV s	50.01 s^{-1}	0.006 mV	199.98 s^{-1}	99.99 Hz			

In numerical computations, four main dynamic indicators are involved [9, 28]: oscillation frequency (FR), oscillation amplitude (AM), average discharge rate (ADR) of the nucleus, and the triggered average discharge rate (TADR) of the PPN. The analytical techniques for these indicators can be found in our previous research [9]. In particular, we carry out a quick Fourier transformation on the time series data of ϕ to acquire the power spectral density, and subsequently designate the frequency of the highest peak as the FR of the model. The AM is characterized as the difference obtained by subtracting the minimum value from the maximum value of the time-series data of ϕ within a single cycle. The ADR for a particular population is derived by taking the arithmetic mean of the time-series data pertaining to this population across a substantially lengthy time span. The TADR represents the ADR value of the PPN at those pivotal junctures that lie between the oscillatory condition and the stable condition. Additionally, the bifurcation curves in the two-dimensional parameter space (such as Figure 2(A1)) are obtained through simulations using the bifurcation analysis toolbox in MATLAB.

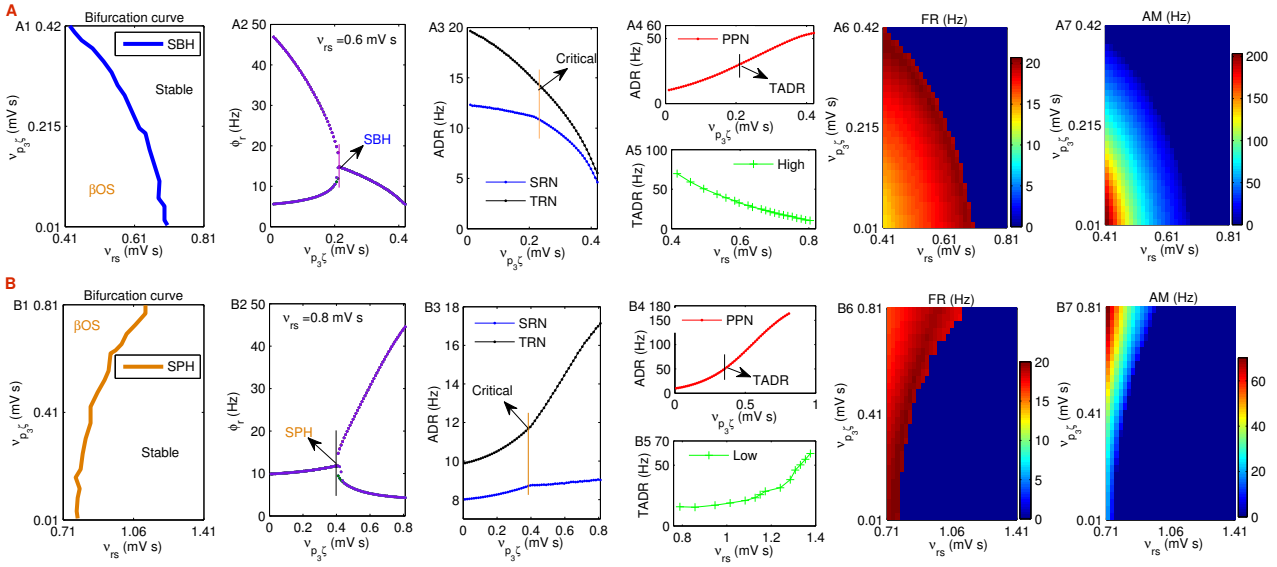

Figure 2. The control effect of the STN-PPN projection on βOS in the thalamic circuit. A: The STN-PPN projection can inhibit βOS through the isolated PPN-TRN pathway (i.e., ν_{sp_3}=0 mV s). A1: The SBH curve simulated in the parameter $(\nu_{rs}, \nu_{p_3\zeta})$ space. A2: A one-dimensional state bifurcation diagram of TRN as a function of $\nu_{p_3\zeta}$. A3: The evolutionary trend of ADR in the thalamic nuclei with the increase of $\nu_{p_3\zeta}$. A4,A5: The evolutionary trends of ADR (A4) and TADR (A5) in PPN. A6,A7: The distributions of FR (A6) and AM (A7) in TRN in the parameter $(\nu_{rs}, \nu_{p_3\zeta})$ space. B: The STN-PPN projection can control βOS through the isolated PPN-SRN pathway (i.e., ν_{rp_3}=0 mV s). B1: The SPH curve simulated in the parameter $(\nu_{rs}, \nu_{p_3\zeta})$ space. B2: A one-dimensional state bifurcation diagram of TRN as a function of $\nu_{p_3\zeta}$. B3: The evolutionary trend of ADR in the thalamic nuclei with the increase of $\nu_{p_3\zeta}$. B4,B5: The evolutionary trends of ADR (B4) and TADR (B5) in PPN. B6,B7: The distributions of FR (B6) and AM (B7) in TRN in the parameter $(\nu_{rs}, \nu_{p_3\zeta})$ space.

3. Main result

3.1. The STN-PPN projection controls βOS of thalamic circuits via two PPN-thalamic pathways

In this section, we primarily focus on the dynamic mechanism by which the STN-PPN projection regulates βOS within the PPN-CTBG1 model. Here, we assume that βOS originates from the thalamic circuit.

3.1.1. Emergence of βOS in PPN-CTBG1 via thalamic coupling

In previous models, we observe that the coupling weights within the thalamic circuit can trigger βOS in the cortical-thalamic network [9]. Similarly, we observe that by altering the coupling strengths within the thalamic circuit, significant βOS emerges in the thalamic nuclei of the PPN-CTBG1 model. Furthermore, we find that βOS in the thalamic circuit might propagate to other circuits.

First, a linear increase in the coupling strength $-\nu_{sr}$ (Figure 3(A1)) within the TRN-SRN projection can induce three distinct states in the oscillatory time series of thalamic nuclei (Figure 3(A2),(A3)): S1 represents the steady state at the maximum discharge rate, and S denotes the

general steady state. Second, we observe that a linear increase in the coupling strength ν_{rs} (Figure3(B1)) within the SRN-TRN projection can also induce three distinct states in the thalamic nuclei (Figure 3(B2)). βOS undergoes transitions between stable states (S and S1) via supercritical Hopf bifurcation (SPH) and subcritical Hopf bifurcation (SBH). Interestingly, we observe that βOS within the thalamic circuit may propagate to other circuits, thereby leading to the emergence of significant βOS in other nuclei of the PPN-CTBG1 model as well (Figure 3(B3)). Furthermore, we utilize the power spectrum to extract the peak oscillation frequency (FR). We observe that the FR in the stable state is 0 Hz Figure 3(C1)), while the FR in the oscillatory state falls within the range of 13–30 Hz (Figure 3(C2),(C3)).

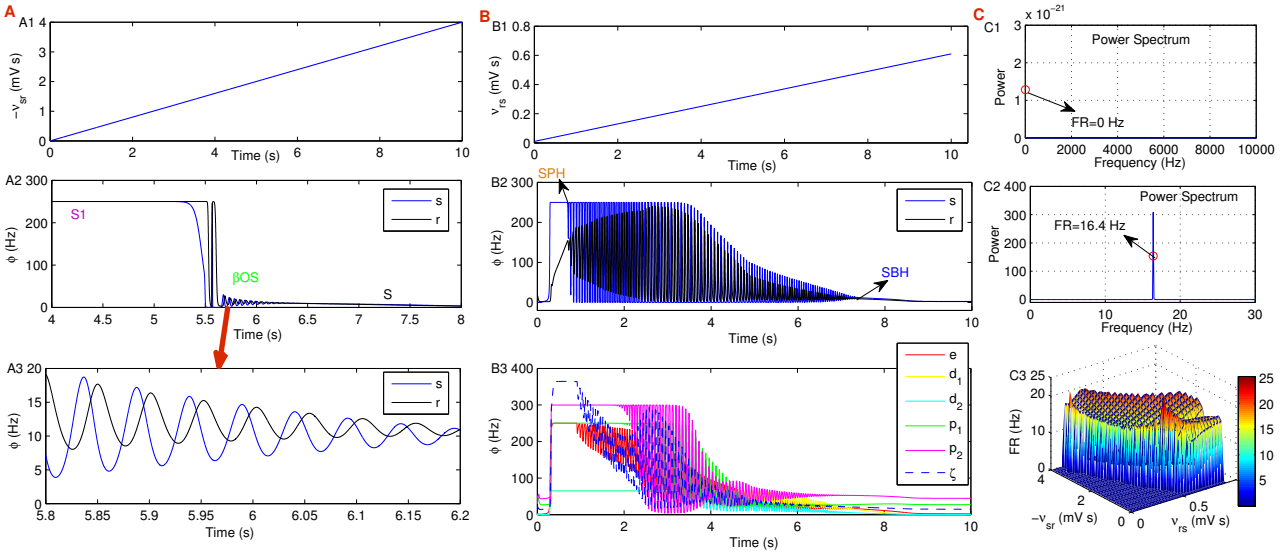

Figure 3. βOS is induced by coupling weights in the thalamic circuitry. A: A linear increase in coupling strength within the TRN-SRN projection (A1) can trigger transitions in the oscillatory time series of thalamic nuclei (A2,A3). S1 represents the steady state at the maximum discharge rate, S denotes the general steady state. B: The transition in the oscillation time series of thalamic nuclei (B2) and those of other nuclei (B3) induced by the linear increase in coupling strength within the SRN-TRN projection (B1). SPH stands for supercritical Hopf bifurcation, and SBH stands for subcritical Hopf bifurcation. C: Frequency analysis of oscillatory time series. C1,C2: Power spectral analysis of peak frequency, which is used as the oscillation frequency (FR) of the model. C3: Three-dimensional FR simulation results in the parameter $(\nu_{rs}, -\nu_{sr})$ space.

Therefore, the thalamic circuit may serve as the origin area of βOS in the PPN-CTBG1 model. Next, we are interested in whether the STN-PPN projection can control βOS within the thalamic circuit through PPN's direct GLU outputs to the thalamus.

3.1.2. STN-PPN modulation of thalamic βOS via two PPN-thalamic GLU Pathways

To investigate the distinct dynamic functions of the PPN-TRN pathway and the PPN-SRN pathway in regulating βOS with as much precision as possible, in this section, we assume that these two pathways exist in isolation within the PPN-CTBG1 model.

In Figure 2(A), we consider the control effect of the STN-PPN projection on βOS in the TRN through the isolated PPN-TRN pathway under the assumption that the PPN-SRN pathway does not exist in the PPN-CTBG1 model (i.e., ν_{sp_3}=0 mV s). First, we obtain the Hopf bifurcation curve in the parameter $(\nu_{rs}, \nu_{p_3\zeta})$ space (Figure 2(A1)). As shown in Figure 2(A1), above the curve lies the stable state, while below the curve is βOS. Therefore, an increase in $\nu_{p_3\zeta}$ can cause βOS to transition to a stable state. That is, the bifurcation curve here is defined as the SBH curve. Figure 2(A2) is a specific state bifurcation diagram. The bifurcation mechanism can be further explained by the changing trend in the average discharge rate (ADR) of thalamic nuclei. An increase in $\nu_{p_3\zeta}$ modulates the ADR of the SRN through the STN-PPN-TRN-SRN pathway. Since the TRN-SRN pathway is inhibitory, the increase in $\nu_{p_3\zeta}$ exerts an inhibitory effect on the SRN. The weakened discharge activation capacity of the SRN further diminishes the excitatory influence of the GLU SRN-TRN pathway on the TRN. Consequently, both the ADR of the SRN and the TRN decrease as $\nu_{p_3\zeta}$ increases (Figure 2(A3)). When the ADRs drop below a critical threshold, βOS is suppressed. Similar to previous studies [9, 28], at the parameter values corresponding to the SBH curve, the PPN exhibits triggered ADR (TADR). We observe that when the ADR of the PPN exceeds its TADR, βOS in the thalamic nuclei is suppressed (Figure 2(A4),(A5)). Therefore, following a similar convention as before [9, 28], we define this TADR at this moment as a high TADR. Finally, we simulate the evolutionary trends of the FR (Figure 2(A6)) and oscillation amplitude (AM) (Figure 2(A7)) within the corresponding parameter space. On the one hand, we observe that the FR falls within the range of 13–30 Hz. On the other hand, consistent with previous studies [9, 32], the parameter regions with higher FR correspond to relatively smaller AM.

In Figure 2(B), we consider the control effect of the STN-PPN projection on βOS in the TRN through the isolated PPN-SRN pathway under the assumption that the PPN-TRN pathway does not exist in the PPN-CTBG1 model (i.e., ν_{rp_3}=0 mV s). The Hopf bifurcation curve is obtained in the parameter $(\nu_{rs}, \nu_{p_3\zeta})$ space (Figure 2(B1)). We observe that the phenomenon associated with βOS occurs above the curve, while the stable state exists below the curve. Therefore, a decrease in the parameter $\nu_{p_3\zeta}$ can suppress βOS. Figure 2(B2) is a specific state bifurcation diagram. In contrast to Figure 2(A1), the bifurcation curve here is defined as the SPH curve. Here, the discharge activity of the SRN is primarily influenced by the excitatory STN-PPN-SRN pathway, while the discharge activity of the TRN is mainly affected by the excitatory STN-PPN-SRN-TRN pathway. Consequently, the ADR of the thalamic nuclei increases with an increase in $\nu_{p_3\zeta}$ (Figure 2(B3)). When the ADR is below its critical threshold, βOS is kept under control. Under such circumstances, the PPN also exhibits the TADR. We observe that when the ADR of the PPN is lower than its TADR, βOS is suppressed (Figure 2(B4),(B5)). Therefore, this TADR at this time is defined as the low TADR. In Figure 2(B6),(B7), we respectively present the evolutionary trends of FR and AM.

Therefore, the STN-PPN projection can control βOS through both the isolated PPN-SRN pathway and the isolated PPN-TRN pathway, with opposite regulatory directions for the Hopf bifurcation. Next, we are interested in the impact on the control pattern of βOS by the STN-PPN projection when both the PPN-SRN pathway and the PPN-TRN pathway coexist in the PPN-CTBG1 model.

3.1.3. PPN-SRN and PPN-TRN pathway interaction modulates Hopf bifurcation and TADR type

In this section, we investigate the impact of the interaction between the PPN-SRN pathway and the PPN-TRN pathway on the regulatory pattern of βOS by the STN-PPN projection.

Figure 4(A1)–(A6) depict the simulated Hopf bifurcation curves in the parameter $(\nu_{rs}, \nu_{p_3\zeta})$ space

when ν_{rp_3} is set to 0.05 times (Figure 4(A1)), 0.1 times (Figure 4(A2)), 0.2 times (Figure 4(A3)), 0.3 times (Figure 4(A4)), 0.5 times (Figure 4(A5)), and 0.8 times (Figure 4(A6)) its default value, respectively. Figure 4(B1)–(B6) presents the analytical results of the PPN's TADR corresponding to Figure 4(A1)–(A6). When ν_{rp_3} is relatively small, the PPN-SRN pathway plays a dominant role in regulating the discharge activity of the thalamic nuclei. Therefore, under these circumstances (Figure 4(A1)–(A3)), the patterns of parameter $\nu_{p_3\zeta}$ controlling βOS are similar to that in Figure 2(B1), and the type of TADR is consistently low (Figure 4(B1)–(B3)). When ν_{rp_3} increases to a certain level, the PPN-TRN pathway gradually takes on a dominant role in regulating the discharge activity of the thalamic nuclei. Consequently, under these circumstances (Figure 4(A4)–(A6)), the patterns of parameter $\nu_{p_3\zeta}$ controlling βOS are similar to that shown in Figure 2(A1), and the type of TADR is consistently high (Figure 4(B4)–(B6)). Therefore, the interaction between the PPN-SRN pathway and the PPN-TRN pathway significantly influences the Hopf bifurcation pattern of βOS controlled by the STN-PPN projection and alters the type of TADR.

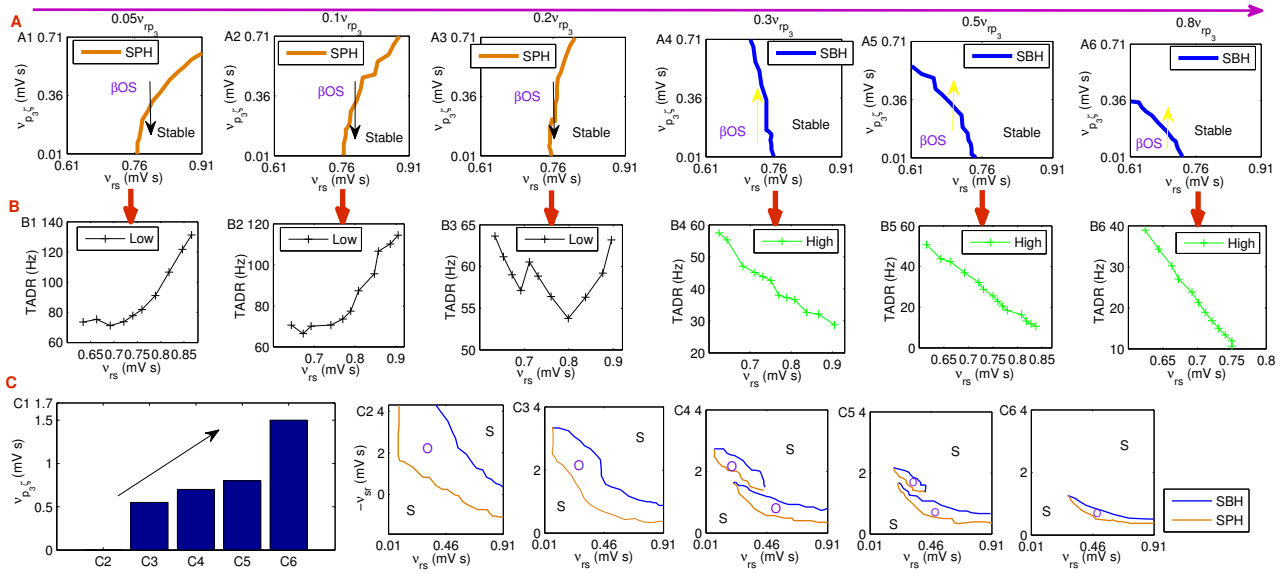

Figure 4. The impact of the relative magnitude of coupling weights on the PPN-SRN pathway and the PPN-TRN pathway on the control of βOS by the STN-PPN projection. A: An increase in coupling strength on the PPN-TRN pathway can cause the SPH curve to evolve into an SBH curve in the parameter $(\nu_{rs}, \nu_{p_3\zeta})$ space. B: As an increase in coupling strength on the PPN-TRN pathway, the type of TADR in PPN evolves from low to high. C: As the coupling strength on the STN-PPN projection increases, the Hopf bifurcation curves shift, and the βOS region gradually shrinks in the parameter $(\nu_{rs}, -\nu_{sr})$ space.

Finally, we examine the impact of the coupling strength on the STN-PPN projection on the Hopf bifurcation curves and the oscillatory regions within the two-dimensional parameter $(\nu_{rs}, -\nu_{sr})$ space. In Figure 4(C1), we sequentially select five different values for $\nu_{p_3\zeta}$. Under these five distinct values, we simulate the Hopf bifurcation curves in the parameter $(\nu_{rs}, -\nu_{sr})$ space (Figure 4(C2)–(C6)), respectively. The area enclosed by the SPH curve and the SBH curve represents the βOS parameter region. We observe that as $\nu_{p_3\zeta}$ increases, both the SPH curve and the SBH curve gradually shorten,

with the SBH curve moving downward progressively, and the βOS parameter region gradually shrinking. Consequently, an increase in parameter $\nu_{p_3\zeta}$ exerts a significant inhibitory effect on the βOS region.

Therefore, the results in Section 3.1 suggest that lesions in the coupling weights of the thalamic circuit may trigger βOS throughout the entire CTBG circuit, while the STN-PPN projection can effectively control βOS through the interaction via the PPN-SRN pathway and the PPN-TRN pathway. There are high and low TADRs in the PPN. The fundamental dynamic mechanisms underlying the origin and regulation of βOS are the SPH and the SBH.

3.2. GLU PPN-EPN control of cortical βOS via SPH and SBH

In this section, we consider the βOS caused by changes in the coupling weights of the cortical circuit, as well as the possible control mechanism of the direct GLU PPN-EPN projection over βOS. Here, we use the PPN-CTBG2 model.

We simulate the Hopf bifurcation curve in the parameter $(\nu_{ee}, -\nu_{ei})$ space (Figure 5(A1)). As expected, with the evolution of the parameters, two states, stable and oscillatory, emerge in the $(\nu_{ee}, -\nu_{ei})$ space. For the convenience of subsequent description, we define the transition between S and βOS (O) as HB1, and the transition between S1 and O as HB2. Since ν_{ee} is an excitatory coupling weight directly acts on EPN, as ν_{ee} increases, the transitions among the three states, S, O, and S1, occur sequentially (Figure 5(A2)). On the other hand, ν_{ei} represents an inhibitory coupling weight, so its effect on the state of EPN is opposite to that of ν_{ee}. Figure 5(A3) presents the corresponding FR analysis results, which shows that all FRs fall within the beta band. Therefore, changes in the coupling weights within the cortical circuitry can trigger βOS. Next, we investigate whether the direct GLU PPN-EPN projection can control βOS within the cortical circuitry.

ν_{ep_3} represents the coupling strength on the PPN-EPN projection. In Figure 5(B1), we simulate Hopf bifurcation curves in the (ν_{ee}, ν_{ep_3}) space. We observe that as ν_{ee} is taken different values, an increase or decrease in ν_{ep_3} could potentially transition βOS into the stable state. Obviously, ν_{ep_3} directly enhances the activation level of EPN (Figure 5(B2),(B4)). When ν_{ee} is relatively small, the activation level of EPN is comparatively low. Under such circumstances, as ν_{ep_3} changes, only two states, O and S, emerge within EPN (Figure 5(B3)). When ν_{ep_3} decreases to a certain extent, a low critical ADR (LCA) appears in Figure 5(B2), and O can transition to S via HB1 (Figure 5(B3)). When ν_{ee} is relatively large, the activation level of EPN is comparatively high. In this case, when ν_{ep_3} is very small, EPN remains in state O. When ν_{ep_3} increases to a certain value, a high critical ADR (HCA) appears in Figure 5(B4), and O transitions to S1 via HB2 (Figure 5(B5)).

Furthermore, we examine the impact of ν_{ep_3} on the bifurcation curves within the $(\nu_{ee}, -\nu_{ei})$ space (Figure 5(C)). As ν_{ep_3} increases, both the HB1 and HB2 curves shift towards the upper left corner and gradually disappear. The O region progressively shrinks, while the S1 region expands. Therefore, from a dynamical perspective, the PPN-EPN projection can suppress O by shifting the Hopf bifurcation points.

Thus, in the PPN-CTBG2 model, the GLU PPN-EPN projection can effectively control βOS in the cortex.

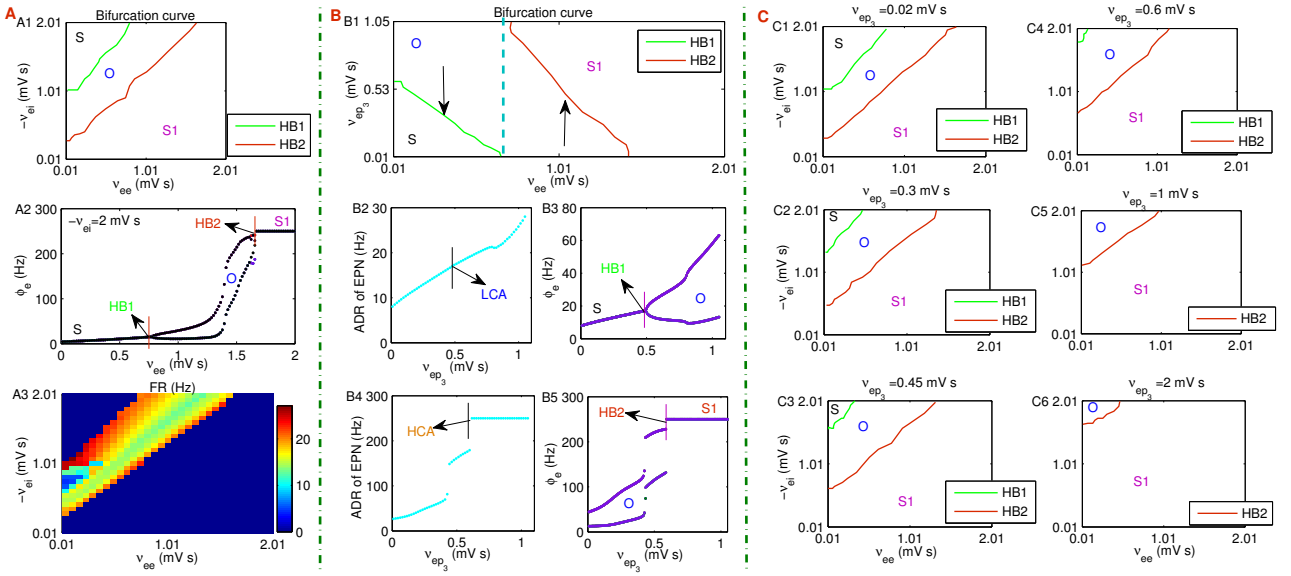

Figure 5. The control effect of the GLU PPN-EPN projection (ν_{ep_3}) on βOS in the cortical circuit. A: Changes in coupling weights within the cortical circuit may trigger significant βOS in the PPN-CTBG2 model. A1: Bifurcation curves simulated in the $(\nu_{ee}, -\nu_{ei})$ space. A2: One-dimensional state bifurcation diagram of EPN as a function of ν_{ee}. A3: The evolutionary trend of FR in the $(\nu_{ee}, -\nu_{ei})$ space. B: The inhibitory effect on βOS caused by the increase or decrease of ν_{ep_3}. B1: Hopf bifurcation curves obtained in the (ν_{ee}, ν_{ep_3}) space. B2,B3: As $\nu_{ee} = 0.1$ mV s, the ADR (B2) and state bifurcation (B3) scenarios of EPN as a function of ν_{ep_3}. B4,B5: As $\nu_{ee} = 1$ mV s, the ADR (B4) and state bifurcation (B5) scenarios of EPN as a function of ν_{ep_3}. C: As an increase in ν_{ep_3}, the evolutionary trends of the Hopf bifurcation curves and the βOS region in the $(\nu_{ee}, -\nu_{ei})$ space.

3.3. PPN-GPi regulation of corticothalamic βOS via GPi-thalamic pathways

In this section, we utilize the PPN-CTBG3 model to investigate the potential role of the PPN-GPi projection in controlling βOS. Here, we assume that βOS originate from the cortical-thalamic circuit. Specifically, we consider three scenarios: the isolated existence of the GPi-SRN pathway in the model, the isolated existence of the GPi-TRN pathway in the model, and the coexistence of both the GPi-SRN and GPi-TRN pathways in the model. $\nu_{p_1p_3}$ represents the coupling strength of the PPN-GPi projection. Figure 6(A) indicates that $\nu_{p_1p_3}$ increases linearly over time.

In the simulation depicted in Figure 6(B), we assume that the GPi-SRN pathway exists in isolation within the PPN-CTBG3 model, i.e., $\nu_{rp_1} = 0$ mV s. Based on the structural analysis of the PPN-CTBG3 model, an increase in $\nu_{p_1p_3}$ primarily affects the ADRs of cortical and thalamic nuclei through three pathways: the PPN-GPi-SRN pathway (SRN), the PPN-GPi-SRN-EPN pathway (EPN), and the PPN-GPi-SRN-EPN-TRN pathway (TRN). Among these three pathways, only the GPi-SRN projection is inhibitory. Therefore, an increase in $\nu_{p_1p_3}$ exerts solely inhibitory effects on cortical and thalamic nuclei (Figure 6(B1)). When $\nu_{p_1p_3}$ is relatively small, the cortical-thalamic circuit is in βOS; when $\nu_{p_1p_3}$ increases to a certain extent, βOS is suppressed (Figure 6(B2)). We further observe that FR increases as $\nu_{p_1p_3}$ increases (Figure 6(B3)).

In the simulation depicted in Figure 6(C), we assume that the GPi-TRN pathway exists in isolation

within the PPN-CTBG3 model, i.e., $\nu_{sp_1} = 0$ mV s. Based on the structural analysis of the PPN-CTBG3 model, an increase in $\nu_{p_1p_3}$ primarily affects the ADRs of cortical and thalamic nuclei through three pathways: the PPN-GPi-TRN-SRN pathway (SRN), the PPN-GPi-TRN-SRN-EPN pathway (EPN), and the PPN-GPi-TRN-SRN-EPN-TRN pathway (TRN). Among these three pathways, both the GPi-TRN projection and the TRN-SRN projection are inhibitory. Therefore, an increase in $\nu_{p_1p_3}$ generally exerts an excitatory effect on the cortical-thalamic circuit (Figure 6(C1)). When $\nu_{p_1p_3}$ is relatively small, the cortical-thalamic circuit is in a stable state; when $\nu_{p_1p_3}$ increases to a certain extent, βOS appears by the SPH (Figure 6(B2)). In this case, the FR decreases as $\nu_{p_1p_3}$ increases (Figure 6(C3)).

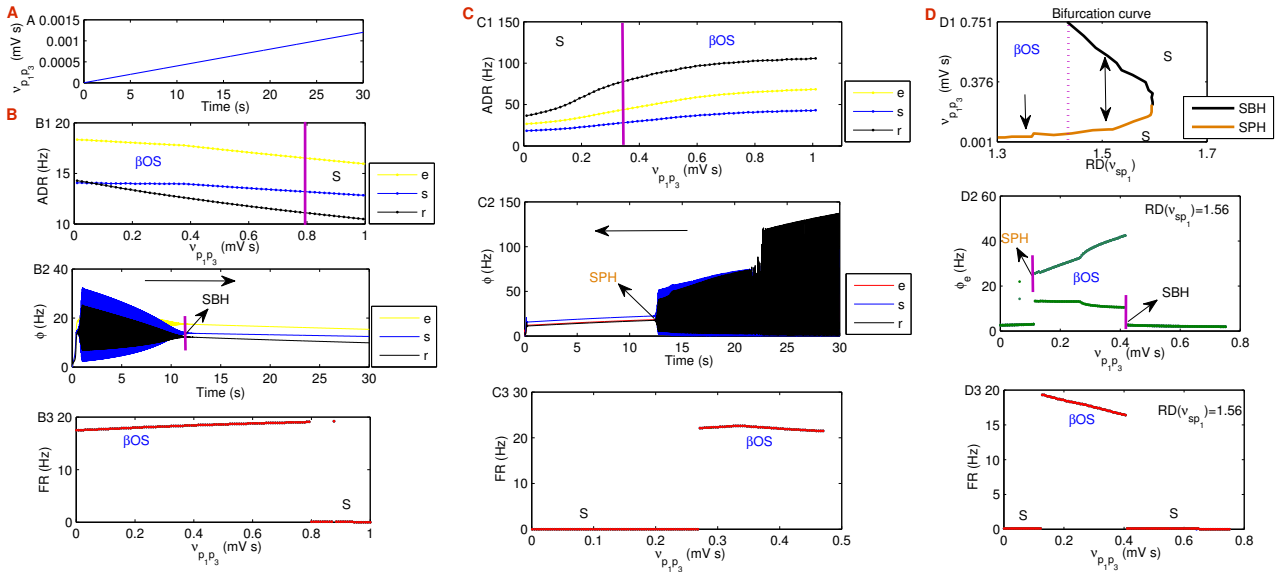

Figure 6. The regulatory effect of the PPN-GPi projection ($\nu_{p_1p_3}$) on βOS in the cortico-thalamic circuit. A: $\nu_{p_1p_3}$ increases linearly with time. B: The increase in parameter $\nu_{p_1p_3}$ can inhibit βOS through the isolated GPi-SRN pathway. B1: The ADRs of the cortical-thalamic circuit decrease as $\nu_{p_1p_3}$ increases. B2: Bifurcation diagram of oscillatory time series in the cortex and thalamic nuclei. B3: The FR of βOS increases as $\nu_{p_1p_3}$ increases. C: The decrease in parameter $\nu_{p_1p_3}$ may control βOS through the isolated GPi-TRN pathway. C1: The ADRs of the cortical-thalamic circuit increase as $\nu_{p_1p_3}$ increases. C2: Bifurcation diagram of oscillatory time series in the cortex and thalamic nuclei. C3: The FR of βOS decreases as $\nu_{p_1p_3}$ increases. D: The impact of the interaction between the two pathways of GPi-thalamus on the control of βOS by the PPN-GPi projection. D1: Hopf bifurcation curves obtained in the parameter $(RD(\nu_{sp_1}), \nu_{p_1p_3})$ space. D2: Regulatory effect of bidirectional Hopf bifurcation on βOS as a function of $\nu_{p_1p_3}$. D3: The evolutionary trend of FR as a function of $\nu_{p_1p_3}$.

Finally, we assume the coexistence of the GPi-SRN pathway and the GPi-TRN pathway in the model to consider how the relative magnitudes of coupling strengths on these two pathways influence the regulation of βOS by the PPN-GPi projection. For example, we use $RD(\nu_{sp_1})$ to represent the ratio of ν_{sp_1} to its default value (Figure 6(D1)). As expected, with the variation of $\nu_{p_1p_3}$, Hopf bifurcation curves can emerge in the parameter $(RD(\nu_{sp_1}), \nu_{p_1p_3})$ space (Figure 6(D1)). Interestingly, in this scenario, the SPH and SBH curves coexist. That is, when $RD(\nu_{sp_1})$ takes an appropriate value, both an

increase or a decrease in $\nu_{p_1p_3}$ can suppress βOS (Figure 6(D2)). In this case, the FR decreases as $\nu_{p_1p_3}$ increases (Figure 6(D3)).

In summary, through the transmission via the GPi-thalamic pathways, the PPN-GPi projection can achieve the Hopf bifurcation transition between βOS and stable state, and appear in the cortical-thalamic circuit. Moreover, under the interaction of the two GPi-thalamic pathways, the SPH and the SBH coexist.

3.4. The GLU PPN-STN projection can effectively control βOS originating in the BG

In this section, we assume that βOS originates in the BG and consider the control effect of the PPN-STN projection on βOS within the BG. $\nu_{\zeta p_3}$ represents the coupling strength of the PPN-STN projection.

Obviously, the GLU PPN-STN projection acts directly on the STN and further influences the state of the GPe through the GLU STN-GPe projection. Therefore, an increase in $\nu_{\zeta p_3}$ significantly elevates the ADR of both the STN and GPe, and the firing states of the STN and GPe rapidly reach the saturated state S1 (Figure 7(A1)). When $\nu_{\zeta p_3}$ is relatively small, the BG can remain in βOS, and when $\nu_{\zeta p_3}$ increases to a certain value, βOS is pushed into the saturated state S1 and thus become controlled (Figure 7(A2)).

Furthermore, we observe the impact of an increase in parameter $\nu_{\zeta p_3}$ on the state regions within the two-dimensional parameter $(\nu_{p_2\zeta}, -\nu_{\zeta p_2})$ space (Figure 7(B)). As $\nu_{\zeta p_3}$ increases, the SBH curve shifts, the βOS region gradually shrinks, and the saturated state S1 region gradually expands. Therefore, the parameter $\nu_{\zeta p_3}$ exerts a significant inhibitory effect on the βOS region.

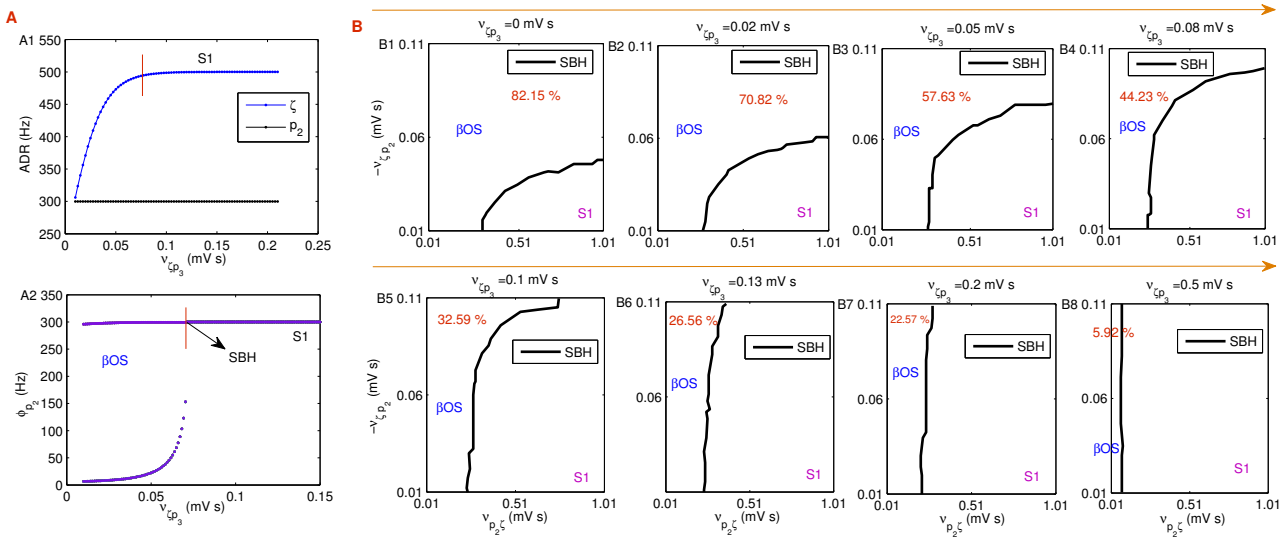

Figure 7. The control effect of the GLU PPN-STN projection ($\nu_{\zeta p_3}$) on βOS in the BG. A: As an increase in $\nu_{\zeta p_3}$, the evolutionary trend of ADR in the STN-GPe circuit (A1) and the state bifurcation diagram of the GPe (A2). B: The impact of the increase in $\nu_{\zeta p_3}$ on the SBH curve and βOS region in the $(\nu_{p_2\zeta}, -\nu_{\zeta p_2})$ space.

Next, we investigate whether the three input projections that have a direct impact on the state of the STN can participate in controlling the βOS in the BG through the PPN-STN pathway (Figure 8).

Figure 8(A) depicts the regulatory effect of GLU EPN-PPN projection (ν_{p_3e}) on βOS in the BG. ν_{p_3e} influences the state of the STN through the PPN-STN pathway and affects the state of the GPe through the PPN-STN-GPe pathway. Since the projections along these pathways are all excitatory, the ADR of the STN-GPe network increases as ν_{p_3e} rises, and can rapidly reach a saturated state S1 (Figure 8(A1)). When ν_{p_3e} is relatively small, the BG is in βOS; when ν_{p_3e} increases to a certain extent, βOS is pushed into S1 by the SBH (Figure 8(A2)). Figure 8(A3),(A4) respectively demonstrate the evolutionary trends of FR and AM in a two-dimensional plane and a three-dimensional space. Among them, FR is around 15 Hz, and AM exhibits a peak band. Thus, the EPN-PPN projection can inhibit βOS via the SBH.

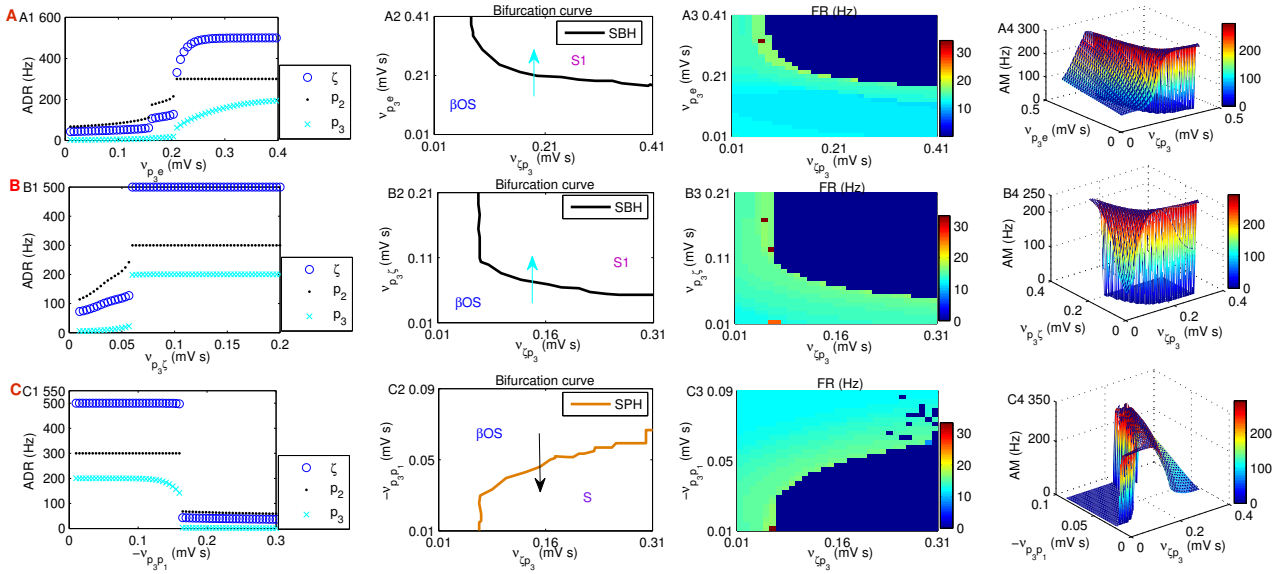

Figure 8. The control effects of the three direct input pathways of PPN on βOS in BG, mediated via the GLU PPN-STN projection. A: The regulatory effect of the EPN-PPN projection (ν_{p_3e}) on βOS. A1: The changing trends of ADR in STN, GPe, and PPN with the increase of parameter ν_{p_3e}. A2: The SBH curve in the parameter ($\nu_{\zeta p_3}$,ν_{p_3e}) space. A3,A4: The evolutionary trends of FR in the two-dimensional parameter space (A3) and AM in the three-dimensional parameter space (A4). B: The control effect of the STN-PPN projection ($\nu_{p_3\zeta}$) on βOS. B1: An increase in parameter $\nu_{p_3\zeta}$ rapidly elevates the ADR of PPN, STN, and GPe, and leads to entry into S1. B2: The evolutionary trend of the SBH curve in the parameter ($\nu_{\zeta p_3}$,$\nu_{p_3\zeta}$) space. B3,B4: The distribution patterns of FR (B3) and AM (B4) in the parameter ($\nu_{\zeta p_3}$,$\nu_{p_3\zeta}$) space. C: The inhibitory effect of the GABA GPi-PPN pathway $\nu_{p_3p_1}$ on βOS in BG. C1: The ADR of PPN, STN, and GPe decreases as parameter $-\nu_{p_3p_1}$ increases. C2,C3,C4: The evolutionary trends of the SPH curve (C2), FR (C3), and AM (C4) in the parameter ($\nu_{\zeta p_3}$,$\nu_{p_3p_1}$) space.

Figure 8(B) illustrates the regulatory effect of GLU STN-PPN projection ($\nu_{p_3\zeta}$) on βOS in the BG. Similar to the analysis in Figure 8(A), $\nu_{p_3\zeta}$ influences the state of the STN through the PPN-STN pathway, and affects the state of the GPe through the PPN-STN-GPe pathway. Therefore, an increase in $\nu_{p_3\zeta}$ generally elevates the activation level of the STN-GPe circuit (Figure 8(B1)). When $\nu_{p_3\zeta}$ is small, the parameter region is in βOS; as $\nu_{p_3\zeta}$ increases, the parameter region rapidly evolves into S1

(Figure 8(B2)). As shown in Figure 8(B3), at the critical points between βOS and S1, FR is relatively large; the farther away from the critical points, the smaller FR becomes. In contrast, the evolutionary trend of AM is basically opposite to that of FR (Figure 8(B4)). So, the STN-PPN projection can control βOS via the SBH.

Figure 8(C) shows the control role of GABA GPi-PPN projection ($\nu_{p_3p_1}$) on βOS in the BG. Clearly, $\nu_{p_3p_1}$ influences the state of the STN through the PPN-STN pathway and affects the state of the GPe through the PPN-STN-GPe pathway. However, since $\nu_{p_3p_1}$ is inhibitory, the increase in $-\nu_{p_3p_1}$ exerts inhibitory effects on the PPN, STN, and GPe (Figure 8(C1)). When $-\nu_{p_3p_1}$ is small, the STN-GPe circuit may be in βOS; when $-\nu_{p_3p_1}$ increases to a certain extent, βOS is pushed into S via the SPH (Figure 8(C2)). Figure 8(C3),(C4) respectively demonstrate the evolutionary trends of FR and AM in a two-dimensional plane and a three-dimensional space. Thus, the GPi-PPN projection can inhibit βOS via the SPH.

In summary, the GLU PPN-STN projection plays a significant role in controlling βOS in the BG, and the three pathways with direct input to the STN can all actively participate in regulating βOS in the BG through the PPN-STN projection. Therefore, based on substantial experimental evidence [12, 24, 33], we reasonably hypothesize that the PPN is an effective target for inhibiting βOS in the BG.

4. Discussion

This study systematically elucidates the dynamic regulatory mechanisms of PPN-related pathways in controlling βOS related to PD, offering insights into the pathological mechanisms of PD and potential therapeutic strategies. By integrating the PPN into the CTBG framework through computational modeling, we reveal that PPN exerts multifaceted modulation on βOS across distinct neural circuits via direct GLU projections, fundamentally advancing existing hypotheses regarding the origin of βOS.

Our findings demonstrate that PPN serves as a critical regulatory hub for βOS through four key pathways. First, the STN-PPN-thalamic projections (PPN-SRN/TRN) exhibit bidirectional Hopf bifurcation control: increasing PPN-TRN coupling suppresses βOS via subcritical Hopf bifurcation SBH, while decreasing PPN-SRN coupling induces βOS suppression through supercritical Hopf bifurcation SPH. Notably, the interaction between these pathways alters the bifurcation type and triggers threshold (TADR) dynamics, highlighting PPN's nuanced control over thalamic oscillations. Second, the PPN-EPN projection demonstrates dual regulatory capacity: in cortical circuits, both increasing and decreasing PPN-EPN coupling can stabilize βOS through SPH/SBH transitions, with triggered activity thresholds (low/high TADR) determining the suppression direction. Third, the PPN-GPi projection modulates cortico-thalamic βOS through GPi-thalamic pathways, where the relative strength of GPi-SRN and GPi-TRN projections determines whether βOS is inhibited (via SBH) or induced (via SPH), with coexistence of both bifurcations under balanced coupling. Finally, the PPN-STN projection directly suppresses BG βOS by elevating STN-GPe activity to saturation, with three direct inputs (EPN-PPN, STN-PPN, GPi-PPN) synergistically enhancing this inhibitory effect.

These results significantly advance the CTBG hypothesis by revealing that PPN integrates with multiple circuits to regulate βOS through coupling-weight-dependent bifurcations. The identification of triggered activity thresholds (TADR) for PPN may provide a dynamical marker for predicting

intervention efficacy. Clinically, our findings support PPN as a promising therapeutic target: the demonstrated suppression of βOS via PPN-related pathways aligns with experimental evidence of PPN-DBS efficacy in alleviating PD axial symptoms [12, 24, 33]. Moreover, the model's prediction that multi-target modulation (e.g., combining PPN-STN and PPN-GPi projections) could enhance βOS suppression offers a rational basis for optimizing DBS parameters.

Although all the parameters of this model are selected from physiologically reasonable ranges (see Table 1), some connection strengths (such as the weight of the PPN-thalamus pathway) lack direct quantitative measurements in the human body and are mainly extrapolated from animal experiments or obtained through reverse fitting. Moreover, there is significant heterogeneity among different PD patients in terms of the degree of PPN neuronal degeneration, receptor expression profiles, and circuit remodeling, while the current model employs a fixed set of parameters and fails to reflect individual differences. In the future, Bayesian parameter calibration or patient-specific LFP data-driven modeling could be used to quantify parameter sensitivity and narrow the uncertainty intervals. In addition, this study has several other limitations. For instance, the model does not explicitly incorporate dopamine dynamics and merely simulates the PD state through static parameters; within the PPN, it does not distinguish the independent roles of cholinergic and GLU subpopulations; and it fails to account for cortical spatial heterogeneity and interactions in non-beta frequency bands (such as gamma and theta bands), among others.

Future work should validate these computational predictions through multimodal experiments combining electrophysiology, optogenetics, and clinical DBS data. Additionally, extending the model to incorporate neurotransmitter dynamics (e.g., dopamine modulation) and individual anatomical variability could refine personalized treatment strategies. By bridging computational neuroscience and clinical neurology, this study might lay the groundwork for targeting PPN-related circuits as a precision medicine approach for PD.

5. Conclusions

The main findings of this paper are summarized as follows: 1) A unified computational model (CTBGP) integrating the PPN and the cortico-thalamic-basal ganglia circuit has been constructed. 2) βOS can arise independently within the cortico-thalamic or BG circuits, and their existence depends on specific combinations of connection strengths. 3) The PPN-cortical projections can either promote or inhibit βOS by enhancing cortical excitability. 4) The PPN-STN GLU projection significantly suppresses pathological βOS within the BG. 5) The STN-PPN feedback connection modulates the activity of the PPN itself, achieving indirect regulation of the oscillatory stability within the CTBG circuit. 6) The projection from PPN to GPi is capable of exerting bidirectional control over βOS via a pair of inhibitory indirect routes. 7) In the parameter combination space, the connection strengths related to the PPN can shift the Hopf bifurcation boundary, thereby regulating the initiation and maintenance of βOS.

Use of AI tools declaration

The authors declare they have not used Artificial Intelligence (AI) tools in the creation of this article.

Acknowledgments

The National Science Foundation of China (Grant No. 11602092); the Natural Science Foundation of Hubei Province, China (Grant No. 2018CFB628); the China Postdoctoral Science Foundation (No. 2018M632184).

Conflict of interest

The authors declare there is no conflict of interest.

References

1. D. Su, Y. Cui, C.He, P. Yin, R. Bai, J. Zhu, et al., Projections for prevalence of Parkinson's disease and its driving factors in 195 countries and territories to 2050: Modelling study of Global Burden of Disease Study 2021, *BMJ*, **388** (2025), 080952. http://doi.org/10.1136/bmj-2024-080952
2. M. F. Hnazaee, V. Litvak, Investigating cortico-striatal beta oscillations in Parkinson's disease cognitive decline, *Brain*, **146** (2023), 3571–3573. https://doi.org/10.1093/brain/awad273
3. S. Little, P. Brown, The functional role of beta oscillations in Parkinson's disease, *Parkinsonism Relat. Disord.*, **20** (2014), 44–48. https://doi.org/10.1016/S1353-8020(13)70013-0
4. E. Belova, U. Semenova, A. Gamaleya, A. Tomskiy, A. Sedov, Excessive α-β oscillations mark enlarged motor sign severity and Parkinson's disease duration, *Mov. Disord.*, **38** (2023), 1027–1035. https://doi.org/10.1002/mds.29393
5. S. J. van Albada, P. A. Robinson, Mean-field modeling of the basal ganglia-thalamocortical system. I: Firing rates in healthy and parkinsonian states, *J. Theor. Biol.*, **257** (2009), 642–663. https://doi.org/10.1016/j.jtbi.2008.12.018
6. S. J. van Albada, R. T. Gray, P. M. Drysdale, P. A. Robinson, Mean-field modeling of the basal ganglia-thalamocortical system. II: dynamics of parkinsonian oscillations, *J. Theor. Biol.*, **257** (2009), 664–688. https://doi.org/10.1016/j.jtbi.2008.12.013
7. M. Caiola, M. H. Holmes, Model and analysis for the onset of parkinsonian firing patterns in a simplified basal ganglia, *Int. J. Neural Syst.*, **29** (2019), 1850021. https://doi.org/10.1142/S0129065718500211
8. Z. Wang, B. Hu, L. Zhu, J. Lin, M. Xu, D. Wang, Hopf bifurcation analysis for Parkinson oscillation with heterogeneous delays: A theoretical derivation and simulation analysis, *Commun. Nonlinear Sci. Numer. Simul.*, **114** (2022), 106614. https://doi.org/10.1016/j.cnsns.2022.106614
9. B. Hu, X. Wang, S. Lu, X. Ying, A study of bidirectional control of Parkinson's beta oscillations by basal ganglia, *Chaos Solitons Fractals*, **195** (2025), 116267. https://doi.org/10.1016/j.chaos.2025.116267
10. K. Santhosh, P. P. Dev, B. J. A, Z. Lynton, P. Das, E. Ghaderpour, A modified Gray Wolf Optimization algorithm for early detection of Parkinson's disease, *Biomed. Signal Process. Control*, **109** (2025), 108061. https://doi.org/10.1016/j.bspc.2025.108061

11. G. Marano, S. Rossi, E. M. Marzo, A. Ronsisvalle, L. Artuso, G. Traversi, et al., Writing the future: Artificial intelligence, handwriting, and early biomarkers for Parkinson's disease diagnosis and monitoring, *Biomedicines*, **13** (2025), 1764. https://doi.org/10.3390/biomedicines13071764
12. P. K. Sharma, S. Gentleman, D. T. Dexter, I. S. Pienaar, Stereological analysis of cholinergic neurons within bilateral pedunculopontine nuclei in health and when affected by Parkinson's disease, *Brain Pathol.*, **35** (2025), 70011. https://doi.org/10.1111/bpa.70011
13. N. J. Ray, R. A. Lawson, S. L. Martin, H. P. Sigurdsson, J. Wilson , B. Galna, et al., Free-water imaging of the cholinergic basal forebrain and pedunculopontine nucleus in Parkinson's disease, *Brain*, **146** (2023), 1053–1064. https://doi.org/10.1093/brain/awac127
14. C. E. Craig, N. J. Jenkinson, J. S. Brittain, M. J. Grothe, L. Rochester, M. Silverdale, et al., Pedunculopontine nucleus microstructure predicts postural and gait symptoms in Parkinson's disease, *Mov. Disord.*, **35** (2020), 1199–1207. https://doi.org/10.1002/mds.28051
15. K. Yu, Z. Ren, Y. Hu, S. Guo, X. Ye, J. Li, et al., Efficacy of caudal pedunculopontine nucleus stimulation on postural instability and gait disorders in Parkinson's disease, *Acta Neurochir.*, **164** (2022), 575–585. https://doi.org/10.1007/s00701-022-05117-w
16. A. Davin, S. Chabardès, A. Devergnas, C. Benstaali, C. N. Gutekunst, O. David, et al., Excessive daytime sleepiness in a model of Parkinson's disease improved by low-frequency stimulation of the pedunculopontine nucleus, *npj Parkinson's Dis.*, **9** (2023), 9. https://doi.org/10.1038/s41531-023-00455-7
17. J. Bourilhon, C. Olivier, H. You, A. Collomb-Clerc, D. Grabli, H. Belaid, et al., Pedunculopontine and cuneiform nuclei deep brain stimulation for severe gait and balance disorders in Parkinson's disease: interim results from a randomized double-blind clinical trial, *J. Parkinson's Dis.*, **12** (2021), 639–653. https://doi.org/10.3233/jpd-212793
18. X. Geng, J. Xie, X. Wang, X. Wang, X. Zhang, Y. Hou, et al., Altered neuronal activity in the pedunculopontine nucleus: An electrophysiological study in a rat model of Parkinson's disease, *Behav. Brain Res.*, **305** (2016), 57–64. https://doi.org/10.1016/j.bbr.2016.02.026
19. I. T. French, K. A. Muthusamy, A review of the pedunculopontine nucleus in Parkinson's disease, *Front. Aging Neurosci.*, **10** (2018), 99. https://doi.org/10.3389/fnagi.2018.00099
20. E. E. Benarroch, Pedunculopontine nucleus: Functional organization and clinical implications, *Neurology*, **80** (2013), 1148–1155. https://doi.org/10.1212/WNL.0b013e3182886a76
21. N. E. Chambers, K. Lanza, C. Bishop, Pedunculopontine nucleus degeneration contributes to both motor and non-motor symptoms of Parkinson's disease, *Front. Pharmacol.*, **10** (2020), 1494. https://doi.org/10.3389/fphar.2019.01494
22. A. Capozzo, T. Florio, R. Cellini, U. Moriconi, E. Scarnati, The pedunculopontine nucleus projection to the parafascicular nucleus of the thalamus: An electrophysiological investigation in the rat, *J. Neural Transm.*, **110** (2003), 733–747. https://doi.org/10.1007/s00702-003-0820-1
23. N. K. Gut, P. Winn, The pedunculopontine tegmental nucleus-A functional hypothesis from the comparative literature, *Mov. Disord.*, **31** (2016), 615–624. https://doi.org/10.1002/mds.26556

24. S. Breit, L. Milosevic, G. Naros, I. Cebi, D. Weiss, A. Gharabaghi, Structural-functional correlates of response to pedunculopontine stimulation in a randomized clinical trial for axial symptoms of Parkinson's disease, *J. Parkinson's Dis.*, **13** (2023), 563–573. https://doi.org/10.3233/JPD-225031

25. P. A. Pahapill, A. M. Lozano, The pedunculopontine nucleus and Parkinson's disease, *Brain*, **123** (2000), 1767–1783. https://doi.org/10.1093/brain/123.9.1767

26. P. A. Robinson, C. J. Rennie, J. J. Wright, P. D. Bourke, Steady states and global dynamics of electrical activity in the cerebral cortex, *Phys. Rev. E*, **58** (1998), 3557–3571. https://doi.org/10.1103/PhysRevE.58.3557

27. P. A. Robinson, C. J. Rennie, D. L. Rowe, Dynamics of large-scale brain activity in normal arousal states and epileptic seizures, *Phys. Rev. E*, **65** (2002), 041924. https://doi.org/10.1103/PhysRevE.65.041924

28. M. Chen, D. Guo, T. Wang, W. Jing, Y. Xia, P. Xu, et al., Bidirectional control of absence seizures by the basal ganglia: A computational evidence, *PLoS Comput. Biol.*, **10** (2014), 1003495. https://doi.org/10.1371/journal.pcbi.1003495

29. M. Chen, D. Guo, M. Li, T. Ma, S. Wu, J. Ma,, et al., Critical roles of the direct GABAergic pallido-cortical pathway in controlling absence seizures, *PLoS Comput. Biol.*, **11** (2015), e1004539. https://doi.org/10.1371/journal.pcbi.1004539

30. B. Hu, J. Zhao, Y. Ao, X. Cai, The possible role of electromagnetic induction in the regulation of absence seizures: evidence from a computational model, *Nonlinear Dyn.*, **113** (2025), 2711–2728. https://doi.org/10.1007/s11071-024-10345-z

31. Y. Yu, H. Zhang, L. Zhang, Q. Wang, Dynamical role of pedunculopntine nucleus stimulation on controlling Parkinson's disease, *Phys. A: Stat. Mech. Appl.*, **525** (2019), 834–848. https://doi.org/10.1016/j.physa.2019.04.016

32. B. Hu, M. Xu, L. Zhu, J. Lin, Z. Wang, D. Wang, et al., A bidirectional Hopf bifurcation analysis of Parkinson's oscillation in a simplified basal ganglia model, *J. Theor. Biol.*, **536** (2022), 110979. https://doi.org/10.1016/j.jtbi.2021.110979

33. V. Witzig, R. Pjontek, S. K. H. Tan, J. B. Schulz, F. Holtbernd, Modulating the cholinergic system-Novel targets for deep brain stimulation in Parkinson's disease, *J. Neurochem.*, **169** (2025), 16264. https://doi.org/10.1111/jnc.16264

Appendix

Following a sequence of logical and appropriate manipulations of Eqs (2.1) and (2.4), we are able to derive a set of first-order differential equations that delineate the CTBGP models depicted in Figure 1. First, Eq (2.4) describes the propagation characteristics of the potential wave in the EPN, and it takes the form of a second-order damped harmonic oscillator equation. By introducing an auxiliary variable $\dot{\phi}_e(t) = \frac{d\phi_e(t)}{dt}$, it can be equivalently rewritten as two first-order equations. Second, for all nuclei, their membrane potential dynamics are described by second-order linear filters (Eqs (2.1) and (2.2)), and incorporate firing rate nonlinearity (Eq (2.3)) as well as multi-input coupling terms, rendering the overall system strongly nonlinear. By defining the state vector $\mathbf{V}(t) = [V_e(t), V_r(t), V_s(t), V_{p_1}(t), V_{p_2}(t), V_\zeta(t), V_{d_1}(t), V_{d_2}(t), V_{p_3}(t)]^T$ and its derivative $\dot{\mathbf{V}}(t)$ to reduce the

order of all second-order terms, 18 first-order ordinary differential equations describing the membrane potential changes can be obtained. The aforementioned order-reduction method is widely adopted in computational neuroscience for simulating large-scale brain network dynamics, and its mathematical equivalence and numerical stability have been thoroughly validated [5, 28, 31].

Ultimately, for the complete CTBGP model (Figure 1(D)), the coupled equations can be presented in the following manner:

$$
\begin{aligned}
\frac{d\phi_e(t)}{dt} &= \dot{\phi}_e(t),\\
\frac{d\dot{\phi}_e(t)}{dt} &= \gamma_e^2[-\phi_e(t) + P_e(V_e(t))] - 2\gamma_e\dot{\phi}_e(t),\\
\frac{d\mathbf{V}(t)}{dt} &= \dot{\mathbf{V}}(t),\\
\mathbf{V}(t) &= [V_e(t), V_r(t), V_s(t), V_{p_1}(t), V_{p_2}(t), V_\zeta(t), V_{d_1}(t), V_{d_2}(t), V_{p_3}(t)]^T,\\
\frac{d\dot{V}_e(t)}{dt} &= \varphi\psi(v_{ee}\phi_e(t) + v_{ei}P_e(V_e(t)) + v_{es}P_s(V_s(t)) + v_{ep_3}P_{p_3}(V_{p_3}(t)) + v_{ep_2}P_{p_2}(V_{p_2}(t)) - V_e(t)) - (\varphi+\psi)\dot{V}_e(t),\\
\frac{d\dot{V}_r(t)}{dt} &= \varphi\psi(v_{re}\phi_e(t) + v_{rp_3}P_{p_3}(V_{p_3}(t)) + v_{rp_1}P_{p_1}(V_{p_1}(t)) + v_{rs}P_s(V_s(t)) + v_{rp_2}P_{p_2}(V_{p_2}(t)) - V_r(t)) - (\varphi+\psi)\dot{V}_r(t),\\
\frac{d\dot{V}_s(t)}{dt} &= \varphi\psi(v_{se}\phi_e(t) + v_{sp_3}P_{p_3}(V_{p_3}(t)) + v_{sp_1}P_{p_1}(V_{p_1}(t)) + v_{sr}P_r(V_r(t)) - V_s(t) + \varphi_{SI}) - (\varphi+\psi)\dot{V}_s(t),\\
\frac{d\dot{V}_{p_1}(t)}{dt} &= \varphi\psi(v_{p_1d_1}P_{d_1}(V_{d_1}(t)) + v_{p_1p_3}P_{p_3}(V_{p_3}(t)) + v_{p_1p_2}P_{p_2}(V_{p_2}(t)) + v_{p_1\zeta}P_\zeta(V_\zeta(t)) - V_{p_1}(t)) - (\varphi+\psi)\dot{V}_{p_1}(t),\\
\frac{d\dot{V}_{p_2}(t)}{dt} &= \varphi\psi(v_{p_2d_2}P_{d_2}(V_{d_2}(t)) + v_{p_2p_2}P_{p_2}(V_{p_2}(t)) + v_{p_2\zeta}P_\zeta(V_\zeta(t)) - V_{p_2}(t)) - (\varphi+\psi)\dot{V}_{p_2}(t),\\
\frac{d\dot{V}_\zeta(t)}{dt} &= \varphi\psi(v_{\zeta e}\phi_e(t) + v_{\zeta p_3}P_{p_3}(V_{p_3}(t)) + v_{\zeta p_2}P_{p_2}(V_{p_2}(t)) - V_\zeta(t)) - (\varphi+\psi)\dot{V}_\zeta(t),\\
\frac{d\dot{V}_{d_1}(t)}{dt} &= \varphi\psi(v_{d_1e}\phi_e(t) + v_{d_1d_1}P_{d_1}(V_{d_1}(t)) + v_{d_1s}P_s(V_s(t)) - V_{d_1}(t)) - (\varphi+\psi)\dot{V}_{d_1}(t),\\
\frac{d\dot{V}_{d_2}(t)}{dt} &= \varphi\psi(v_{d_2e}\phi_e(t) + v_{d_2d_2}P_{d_2}(V_{d_2}(t)) + v_{d_2s}P_s(V_s(t)) - V_{d_2}(t)) - (\varphi+\psi)\dot{V}_{d_2}(t),\\
\frac{d\dot{V}_{p_3}(t)}{dt} &= \varphi\psi(v_{p_3p_1}P_{p_1}(V_{p_1}(t)) + v_{p_3\zeta}P_\zeta(V_\zeta(t)) + v_{p_3e}\phi_e(t) - V_{p_3}(t)) - (\varphi+\psi)\dot{V}_{p_3}(t).
\end{aligned}
$$

To specifically investigate the mechanism by which relevant projections of PPN control βOS in different circuits, we assume that the following pathways in the CTBGP1 model (Figure 1(A)) are severed: the GPi-SRN pathway, the GPi-TRN pathway, the EPN-PPN pathway, and the PPN-EPN pathway. In the CTBGP2 model (Figure 1(B)), the following pathways are severed: the GPi-SRN pathway, the GPi-TRN pathway, the PPN-SRN pathway, the PPN-TRN pathway, and the EPN-PPN pathway. In the CTBGP3 model (Figure 1(C)), the direct communication pathways between PPN and the cortico-thalamic circuit are severed: the PPN-SRN pathway, the PPN-TRN pathway, the PPN-EPN pathway, and the EPN-PPN pathway.